ACS APPLIED MATERIALS & INTERFACES

Research Article

www.acsami.org

Tuning the Electronic Structure of Graphene by Molecular Dopants: Impact of the Substrate

Christos Christodoulou,[†,∇] Angelos Giannakopoulos,[‡,∇] Giovanni Ligorio,[†] Martin Oehzelt,[†,§] Melanie Timpel,[†] Jens Niederhausen,[†] Luca Pasquali,[‖,⊥,#] Angelo Giglia,[⊥] Khaled Parvez,[¶] Klaus Müllen,[¶] David Beljonne,[*,‡] Norbert Koch,[*,†] and Marco V. Nardi[†]

[†]Humboldt-Universität zu Berlin, Institut für Physik, Brook-Taylor-Straße 6, 12489 Berlin, Germany
[‡]Laboratory for Chemistry of Novel Materials, University of Mons, Place du Parc 20, 7000, Mons, Belgium
[§]Helmholtz-Zentrum Berlin für Materialen und Energie GmbH, Albert Einstein Strasse 16, 12489, Berlin, Germany
[‖]University of Modena e Reggio Emilia, Engineering Department, "E. Ferrari", Via Vigolese 905, 41125, Modena, Italy
[⊥]IOM-CNR, Area Science Park, SS 14 Km, 163.5, 34149, Basovizza, Trieste, Italy
[#]Department of Physics, University of Johannesburg, PO Box 524, Auckland Park, 2006, South Africa
[¶]Max Planck Institute für Polymerforschung, Ackermanweg 10, 55128, Mainz, Germany

Supporting Information

ABSTRACT: A combination of ultraviolet and X-ray photoelectron spectroscopy, X-ray absorption spectroscopy, and first principle calculations was used to study the electronic structure at the interface between the strong molecular acceptor 1,3,4,5,7,8-hexafluorotetracyano-naphthoquinodimethane (F_6TCNNQ) and a graphene layer supported on either a quartz or a copper substrate. We find evidence for fundamentally different charge redistribution mechanisms in the two ternary systems, as a consequence of the insulating versus metallic character of the substrates. While electron transfer occurs exclusively from graphene to F_6TCNNQ on the quartz support (p-doping of graphene), the Cu substrate electron reservoir induces an additional electron density flow to graphene decorated with the acceptor monolayer. Remarkably, graphene on Cu is n-doped and remains n-doped upon F_6TCNNQ deposition. On both substrates, the work function of graphene increases substantially with a F_6TCNNQ monolayer atop, the effect being more pronounced (~1.3 eV) on Cu compared to quartz (~1.0 eV) because of the larger electrostatic potential drop associated with the long-distance graphene-mediated Cu-F_6TCNNQ electron transfer. We thus provide a means to realize high work function surfaces for both p- and n-type doped graphene.

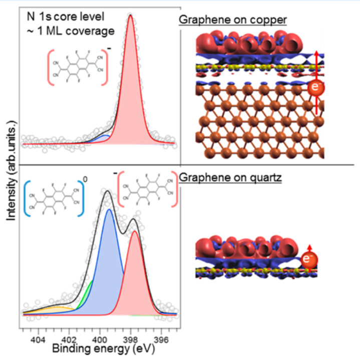

KEYWORDS: *graphene, photoelectron spectroscopy, electrode, doping, molecular acceptor*

INTRODUCTION

Graphene is a scientifically and technologically exceptional material, mainly due to its two-dimensional electronic structure and high charge carrier mobility.[1−3] Graphene's electronic[4] and mechanical properties[5] make this material a serious candidate as transparent electrode in electronic devices such as light emitting diodes,[6] sensors,[7] solar cells,[8] batteries,[9] touchscreens,[10] etc. Among the many methods to produce graphene, e.g., mechanical exfoliation from bulk graphite, growth via chemical vapor deposition (CVD) has proven to provide technologically relevant areas of graphene sheets that are highly crystalline[11] and that can be easily transferred to any substrate of interest.[12] It soon emerged that the key aspect for the success of this 2D material in applications would be the ability to manipulate its electronic structure to suit the application needs. Hence, other materials might be paired with graphene to achieve this goal. In this study, we focus on noncovalent functionalization of graphene[13−19] using small molecules deposited on this 2D surface in ultrahigh vacuum. Noncovalent functionalization does not disrupt the sp^2 bonding network of graphene, allowing it to retain its highly desired electronic, mechanical, and thermal properties, and furthermore, it gives enhanced variability for interface tuning in thin film devices. To improve the performance of graphene as an electrode, modification of its work function is required to match the relevant frontier energy levels of the semiconductor to achieve as low as possible charge injection barriers. One way to increase the work function of metal electrodes in order to improve hole injection consists of depositing a molecular acceptor monolayer.[20]

In the present study, 1,3,4,5,7,8-hexafluoro-tetracyano-naphthoquinodimethane (F_6TCNNQ; see Figure 1 for

Received: June 1, 2015
Accepted: August 17, 2015
Published: August 17, 2015

DOI: 10.1021/acsami.5b04777
ACS Appl. Mater. Interfaces 2015, 7, 19134−19144

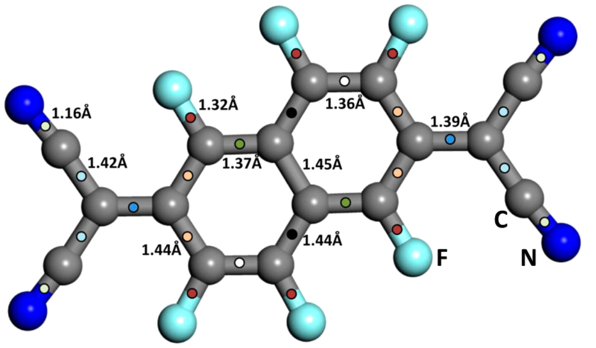

Figure 1. Chemical structure of the molecular acceptor F_6TCNNQ in a neutral state. The bond lengths are displayed. Equivalent bonds are marked with the same color dots. Carbon (C) atoms in gray, nitrogen (N) atoms in blue, and fluorine (F) atoms in cyan.

chemical structure) was used because of its higher molecular weight compared to the very frequently used tetrafluortetracyanoquinodimethane (F_4TCNQ)[14,21] which results in better processability in vacuum and stability in devices. It also has a sublimation temperature of 180−200 °C, which is higher than that of F_4TCNQ (135−145 °C).[22] In another context, F_6TCNNQ has been used as a p-dopant to control the threshold voltage and the ON/OFF ratio of organic transistors.[23]

In a previous study, it was shown that the work function of graphene-on-quartz can be increased by a moderately strong molecular acceptor,[18] rendering graphene transferred on a quartz support a universally applicable hole injection transparent electrode. Using ultraviolet and X-ray photoemission spectroscopy (UPS and XPS) and X-ray absorption spectroscopy (XAS), combined with first principle calculations, the mechanism of the work function increase was identified as being due to electron transfer from graphene to the acceptor, with only a fraction of the molecules in the acceptor monolayer being charged. In the present contribution, we attend to the role played by the support, i.e., graphene-on-quartz (G/Qu) versus graphene-on-copper (G/Cu), on the electronic density rearrangement at the F_6TCNNQ−graphene interface. We separate the work function increase into two contributions: (a) doping of the graphene sheet causing energy level shifts inside the graphene layer and (b) interface dipole formation at the interface between graphene and the molecular layer. We find strong indications that a different support for graphene results in a particular charge transfer (CT) mechanism, rooted in different charge redistribution among the three components involved.

RESULTS AND DISCUSSION

The evolution of the valence region spectra of G/Qu and G/Cu upon sequential deposition of F_6TCNNQ is depicted in Figure 2. Figure 2a,d shows the evolution of the secondary electron cutoff (SECO) spectra up to a nominal thickness (θ) of 5 nm. From these, a molecule-induced work function (Φ) increase of 1.0 eV (G/Cu) and 1.3 eV (G/Cu) up to θ = 0.4 nm and a saturation for further deposition are assessed. The saturated Φ for G/Qu and G/Cu is 5.5 and 5.65 eV, respectively.

A rigid shift (ΔE) of ΔE = 0.6 eV toward lower binding energy (BE) of the graphene energy levels is observed upon the initial deposition of θ = 0.2 nm F_6TCNNQ on G/Qu, as highlighted by the red dashed lines in Figure 2b. This ΔE reflects surface CT doping of graphene due to withdrawal of electrons from the graphene layer by the accepting molecules.[13,24−26] In photoelectron spectroscopy, thermodynamic equilibrium requires the Fermi level of the sample to be at the same level as the Fermi level of the detector, since they are electronically connected. The Fermi level is the reference level (E_F) in PES and is set to 0 eV. When electrons flow from graphene's valence band to the molecular acceptor, the Fermi level of graphene moves downward with respect to the Dirac Point. The downward shifted E_F is set to 0 eV again, after thermodynamic equilibrium is established between graphene and detector. This is manifested as an upward shift of all the

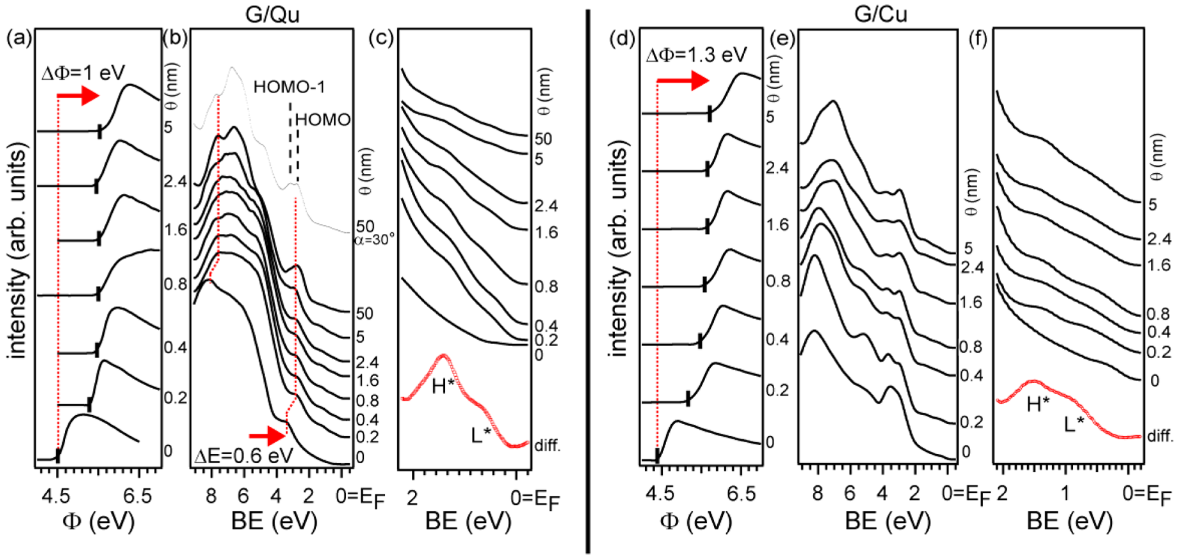

Figure 2. Evolution of the valence electronic structure as a function of F_6TCNNQ deposited on graphene-on-quartz (G/Qu) and graphene-on-copper (G/Cu): evolution of the SECO onset (Φ corresponds to the work function) for (a) G/Qu and (d) G/Cu; evolution of the valence band structure for (b) G/Qu and (e) G/Cu; (c) and (f) show a zoom of the valence band spectra close to the Fermi level (E_F) for G/Qu and G/Cu, respectively. In (b), the valence band spectrum at coverage θ = 50 nm was additionally collected at an electron takeoff angle of 30°. In (c) and (f), the red spectrum shows the valence band spectrum at θ = 0.4 nm after subtraction of the graphene substrate background spectrum.

DOI: 10.1021/acsami.5b04777
ACS Appl. Mater. Interfaces 2015, 7, 19134−19144

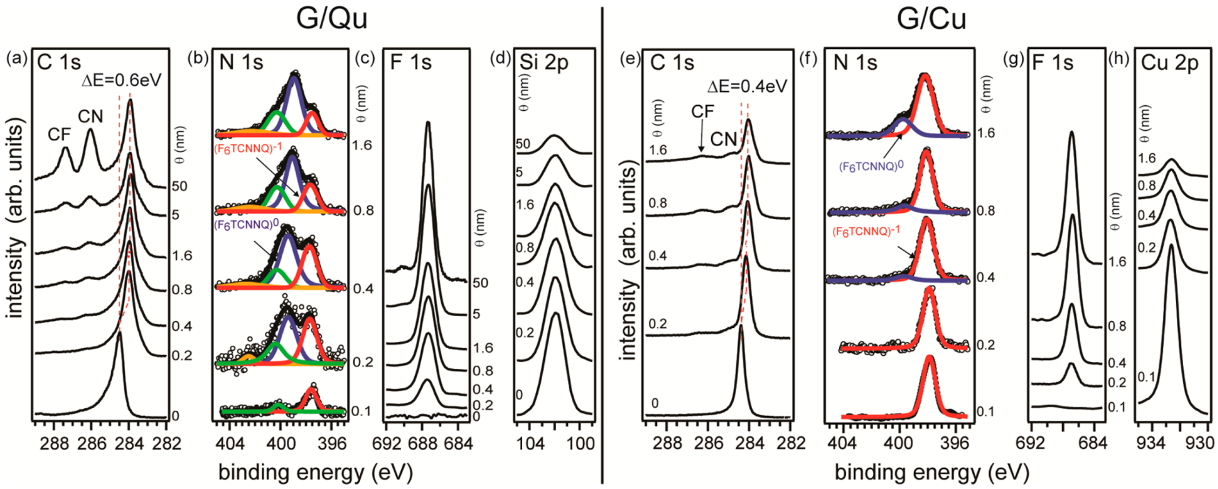

Figure 3. Evolution of the core level spectra of (a) C 1s, (b) N 1s, (c) F 1s, and (d) Si 2p with respect to the thickness of F_6TCNNQ for graphene-on-quartz (G/Qu) and (e) C 1s, (f) N 1s, (g) F 1s, and (h) Cu 2p for graphene-on-copper (G/Cu). The N 1s core level spectra were deconvoluted to the underlying components.

energy levels in graphene, with respect to the new location of the Fermi level. It is difficult to quantitatively assess the corresponding energy shift in the case of G/Cu, as the spectrum is dominated by the photoelectron signal from the underlying Cu support (Figure 2e), yet it seems the effect is much weaker.

From inspection of the spectra in Figure 2b,e, starting from a rather early stage of growth, the HOMO feature of F_6TCNNQ is noticeable around 2.8 eV BE, as expected for the neutral molecule. Moreover, for both G/Qu and G/Cu substrates, two peaks, labeled as H* and L* with their peak maxima located at BE ∼1.5 and ∼0.6 eV, respectively, are evident closer to E_F. These features can be better seen in Figure 2c,f, which represents a zoom of the valence region close to E_F. Similar electronic states have been reported for F_4TCNQ deposited on Au[20] and graphene epitaxially grown on SiC(0001)[13] and were attributed to the (partially) populated former LUMO and the relaxed former HOMO levels of the neutral molecule. The respective red spectra in Figure 2c,f show these two peaks H* and L* after subtraction of the graphene background spectrum for the respective film spectra (with θ = 0.4 nm). The energy separation of these states is ∼0.9 eV, which is much lower than the optical gap of the neutral molecular film (measured to be 2.1 eV). Such a drastic reduction in the energy gap indicates a strong interaction between the molecule and the substrate.[27]

The fact that Φ saturates after θ = 0.4 nm for both graphene/substrate systems (G/Qu and G/Cu) suggests that at this coverage the monolayer of F_6TCNNQ on graphene is completed. The additional presence of H* and L* up to multilayer coverage indicates that, after the monolayer is complete, molecular islands form on top of it.

Figure 3 shows the C 1s (a), N 1s (b), F 1s (c), and Si 2p (d) core level spectra of F_6TCNNQ/G/Qu. The maximum of the C 1s core level peak of graphene is initially at 284.5 eV and shifts to 283.9 eV upon deposition of θ = 0.4 nm of the acceptor. Thus, it shifts by the same amount ΔE = 0.6 eV and in the same direction (toward lower binding energy) as the valence spectra in Figure 2. The graphene C 1s core level peak is still quite strong in the spectrum for θ = 5 nm, supporting pronounced multilayer island growth.

Combining the C 1s core level evolution profile with the work function changes (that saturates already at θ = 0.4 nm, where the monolayer is apparently complete) and the presence of H* and L* at multilayer coverage, we can derive that the most probable mechanism of molecular growth is indeed Stranski-Krastanov, where the molecules form a closed monolayer and subsequently islands on top. The F 1s core level signal from the fluorine at the periphery of F_6TCNNQ is at constant BE of 687.4 eV from θ = 0.2 nm up to θ = 5 nm, suggesting no or minimal interaction of the fluorine atoms with the graphene substrate. The Si 2p core level emission stemming from the supporting quartz under the graphene shows no BE shift; hence, we can exclude any interaction or CT occurring between the molecule and the quartz support.

Figure 3 also shows analogous C 1s (e), N 1s (f), F 1s (g), and Cu 2p (h) core level for the G/Cu case. The C 1s core level exhibits a smaller shift of 0.4 eV toward lower BE, compared to the G/Qu case, and no shift of the F 1s core level is observed. The Cu 2p emission from the underlying copper support shows as well no extra features, indicating that the molecule does not interact chemically with the Cu substrate.

The N 1s core level spectra appear more complex, as only one component is expected from the molecular structure. In Figure 3b,f, sequences of spectra for increasing F_6TCNNQ coverages are shown for (G/Qu) and (G/Cu), respectively. The spectra can be deconvoluted into four components. In Figure 3b (G/Qu), the feature at 397.5 eV BE (red color) is assigned to electron enriched N in F_6TCNNQ, very similar to the already reported N 1s core level emission of anionic F_4TCNQ on epitaxially grown graphene on SiC(0001).[13,14] This emission indicates a significant charge accumulation at the cyano groups ($-C{\equiv}N$) of the F_6TCNNQ anion. For submonolayer coverage (θ = 0.1 nm), essentially all molecules in contact with the graphene are in the anionic state. At θ = 0.2 nm, an additional feature at 399.4 eV BE appears, which is attributed to neutral F_6TCNNQ. At this coverage, fitting yields that ca. 50% of the molecules are neutral and ca. 50% are negatively charged. At this (sub)monolayer coverage, neutral and negatively charged molecules thus coexist in the monolayer. Two more features are observable at θ = 0.2 nm, located at 400.5 eV BE (green color) and 402.6 eV BE (orange color); these are attributed to shakeup satellites. Upon increasing coverage, the feature stemming from neutral molecules grows in intensity and shifts toward lower BE (by

<0.4 eV). This can be attributed to the existence of more than one molecular orientation in the multilayers, which translates into different ionization energies.[28]

In Figure 3f, the N 1s core level spectrum for F_6TCNNQ on G/Cu is depicted. In this case, up to θ = 0.4 nm, only one feature is clearly visible (red color) at 397.7 eV BE stemming from negatively charged F_6TCNNQ. Beyond θ = 0.8 nm, the emission stemming from neutral molecules appears at 399.7 eV BE. In contrast to the G/Qu case, a higher fraction of F_6TCNNQ is negatively charged in the (sub)monolayer with neutral molecules starting to appear at a later stage of the deposition, i.e., upon formation of the multilayers. This evidences the important role of the two different graphene supports, i.e., Qu versus Cu.

XAS measurements were used to characterize the (average) orientation of F_6TCNNQ on G/Qu and the CT occurring at the interface between molecule and graphene. XAS spectra of F_6TCNNQ on G/Qu were recorded at two different coverages: (a) less than 0.5 monolayer (i.e., θ = 0.1 nm) and (b) ca. 1 monolayer (i.e., θ = 0.4 nm). The spectra were collected from N K-shell electrons excited to unoccupied molecular orbital (MO) levels. Figure 4 shows the XAS spectra (π* region) collected at five different takeoff angles ψ_c spanning from 0° to 90°. Mainly three principal spectral features were identified at both coverages, labeled as I, II, and III. On the basis of our DFT-simulated absorption spectra shown in Figure 5, we ascribe the main peak at 399.2 eV (labeled as II in Figure 4) to transitions from the N 1s to the $-C{\equiv}N$ π*-antibonding orbital lying within the molecular plane (see inset in Figure 5). Peak I at 396.8 eV and peak III at 400.2 eV are assigned to transitions from N 1s to the π* orbitals of the cyano groups orientated perpendicular to the molecular plane (i.e., z axis).

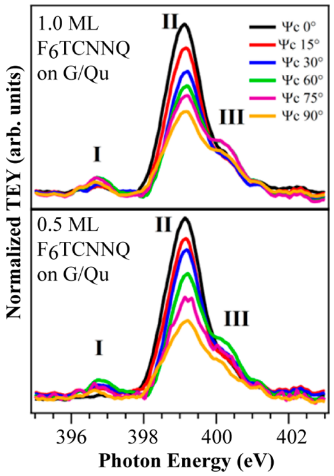

Figure 4. Experimental N K-edge XAS spectra of 0.5 monolayer (ML) (lower panel) and 1.0 ML (upper panel) of F6TCNNQ on G/Qu collected at six different angles ψ_c.

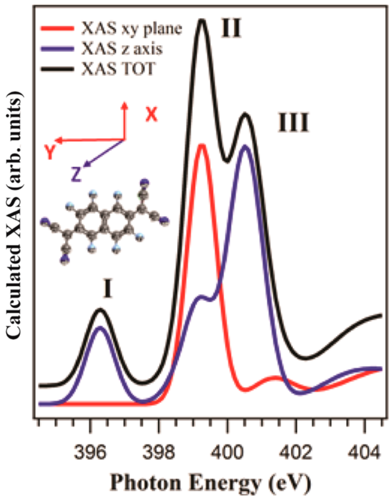

Figure 5. DFT-calculated N K-edge XAS spectra of the F_6TCNNQ molecule. XAS xy plane (red) is the absorption in the xy plane of the molecule; XAS z-axis (blue) is the absorption in the axis perpendicular to the molecule, and XAS TOT (black) is the total absorption.

The main peak II exhibits a strong angular dependence; i.e., it is greatly enhanced when the electric field vector is parallel to the surface plane (i.e., ψ_c = 0°, s-polarization) but largely attenuated when the electric field is almost perpendicular to the surface plane (i.e., ψ_c = 90°, p-polarization), suggesting a planar orientation of the molecule on top of the graphene layer. To better quantify the average orientation of the molecules with respect to the underlying graphene layer, we monitored the intensity of feature II at 399.2 eV collected at six different angles.

Assuming that at the surface the molecules have isotropic azimuthal distribution in the monolayer, the intensity I of a resonance peak corresponding to an excitation into a vector orbital in the used experimental configuration can be described by[29]

$$\frac{I(\theta)}{I(90°)} = [(\varepsilon^2\cos^2\Psi_c + \sin^2\Psi_c)(\sin^2\theta_M\sin^2\theta + \cos^2\theta_M\cos^2\theta) + (\varepsilon^2\sin^2\Psi_c + \cos^2\Psi_c)\sin^2\theta]/[\sin^2\theta_M\sin^2\theta + \cos^2\theta_M\cos^2\theta + \varepsilon^2\sin^2\theta] \quad (1)$$

with θ_M as the grazing incidence angle (θ_M = 10°), ψ_c as the rotation angle of the analysis chamber at the BEAR beamline with the specific setup used for the measurement, ε as the photon ellipticity (ε = 0.1), and θ as the tilt angle to be determined. The best fits using eq 1, assuming θ as a free parameter, are shown in Figure 6, indicative of an average tilt angle (i.e., molecular plane with respect to the substrate plane) of ∼22° and ∼24° for 0.5 monolayer and 1.0 monolayer of F_6TCNNQ on G/Qu, respectively.

In addition to the average tilt angle derived from combined XAS analysis and DFT simulations, we studied any possible variation in the charge state of the molecule when going from the submonolayer (interface) to the multilayer (bulk) regime. For this purpose, we performed DFT calculations considering the molecule in two different situations: the neutral case, when the molecule is not experiencing any CT from the substrate (corresponding to the multilayer) and the case where the molecule is charged with an electron from the underlying graphene. Figure 7 shows simulated XAS spectra in comparison to the experimental XAS measurements performed at two different coverages, namely, 0.5 monolayer (i.e., interface) and a few nanometers (i.e., multilayer). For a better comparison, the absolute energy of the simulated spectra (red and black) were aligned with the corresponding experimental ones. The shape and the relative intensity of the features labeled as I, II, and III were basically not affected by the different charge states of the molecule (i.e., negatively charged or neutral). The only remarkable difference between the two simulated spectra, red

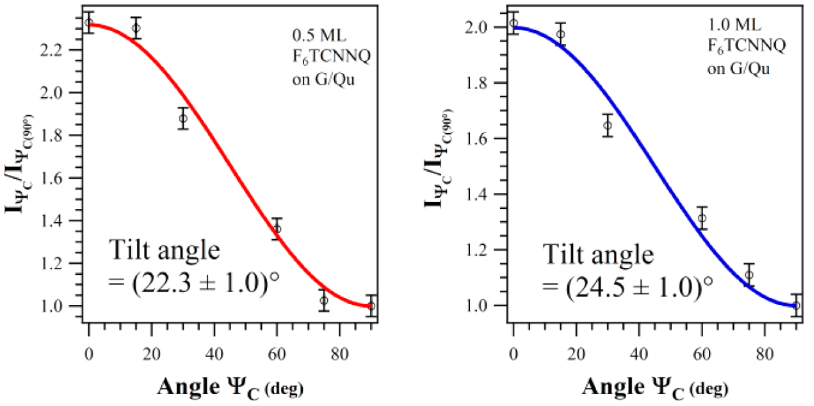

Figure 6. Plots of the relative peak intensities of feature II of F6TCNNQ on G/Qu as a function of the photon incidence angle ΨC. The solid curve corresponds to the best fit of the intensity evolution for 0.5 monolayer (ML) (left panel) and 1.0 ML (right panel).

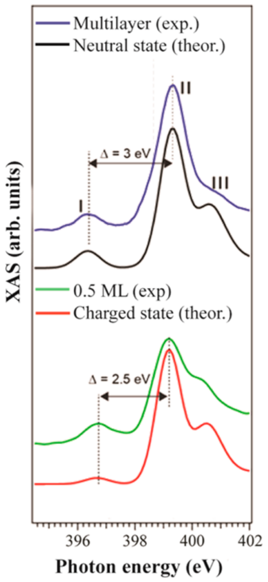

Figure 7. Direct comparison between the experimental N K-edge XAS spectra of F_6TCNNQ on G/Qu and the DFT-calculated spectra of the F_6TCNNQ molecule in the neutral state (black spectrum in the upper part) and negatively charged state (red spectrum in the lower part).

(negatively charged molecule) and black (neutral molecule), is the energy separation between features I and II (2.5 and 3.0 eV, respectively). No appreciable difference, neither in the line shape nor in the relative intensity of the features, can be noted when the experimental and the simulated XAS spectra are compared. However, it can be seen that the energy differences between peaks I and II, experimentally measured at the interface and from the multilayer, are in excellent agreement with the calculated ones, in line with the XPS results further above in which a significant fraction of the F_6TCNNQ molecules in contact with the graphene layer is negatively charged.

First principle calculations were performed in order to better understand the features observed in the valence region spectra recorded in UPS for the F_6TCNNQ/G interface. Due to its highly insulating character, the Qu support should not significantly affect the charge redistribution at the F_6TCNNQ–graphene interface and thus was not implemented in the following simulations. The size of the supercells used for the calculations was $17.1 \times 9.9 \times 30$ Å^3. The interaction energy between graphene and the F_6TCNNQ molecule is 1.05 eV/nm^2, with the dopant lying 3.21 Å over graphene. The nitrogen atoms of the cyano groups are slightly closer to graphene, 3.16 Å, though the difference is small and the molecule is considered planar (Figure S4). Figure 8 shows the partial density of states

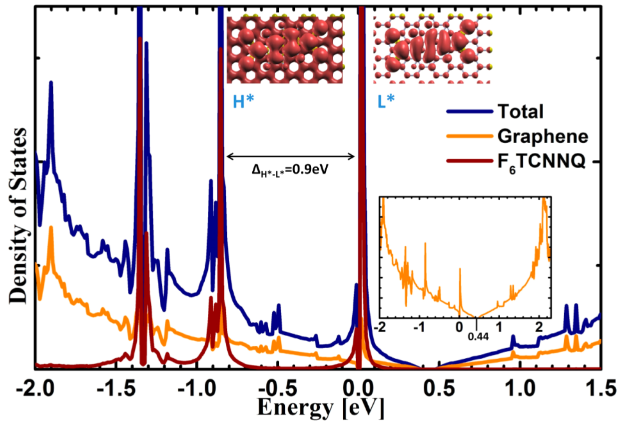

Figure 8. Partial density of states (PDOS) plot for F_6TCNNQ adsorbed on graphene. The orange curve shows the DOS of graphene; the dark red curve shows the DOS of F_6TCNNQ, and the dark blue curve shows the total DOS of the system. The inset plot shows a zoom of the DOS of graphene, indicating the position of the Dirac point. The inset figures show the local density of states (LDOS) of the H* and L* peaks.

(PDOS) of F_6TCNNQ physisorbed on graphene. There is a consistency between theory and experiment in two important aspects: (I) The simulations capture the shift of the Dirac point (E_D) of the F_6TCNNQ/G system toward lower binding energy, $\Delta E_F = 0.44$ eV, as it is also shown by the band structure in Figure 9c. (II) There are two new electronic states below E_F. The $\Delta E_F = 0.44$ eV together with the calculated work function shift, $\Delta\Phi$, of 1.08 eV (the difference in the work functions of F_6TCNNQ physisorbed on graphene and pristine graphene, while the work function is defined as the energy difference between the vacuum level and the Fermi level) are in excellent agreement with experiment and correspond to a vacuum level shift (ΔE_{vac}) of 0.64 eV ($\Delta E_{vac} = \Delta\Phi - \Delta E_F$). To gain further insight, the local density of states (LDOS) was calculated by integrating around the energy of the two new states (see inset figures in Figure 8; L* and H* with integration performed 0.1 eV around the energy of the peaks). The LDOS displays the

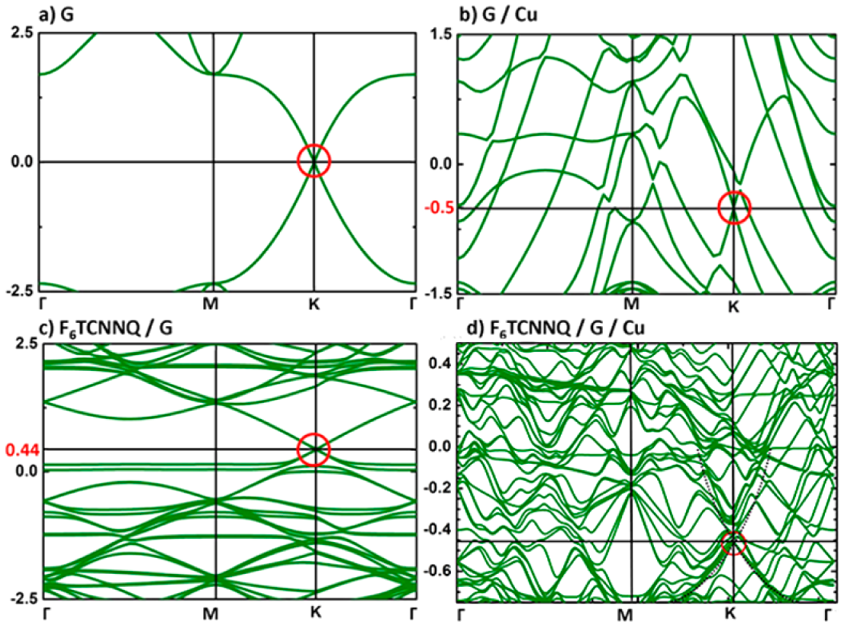

Figure 9. Electronic band structures of (a) graphene (G) and (b) G/Cu unit cells; (c) and (d) show the electronic band structures of F_6TCNNQ adsorbed on top of the supercells displayed in (a) and (b), respectively. The red circles in the figures indicate the position of the Dirac point. The zero energy corresponds to E_F.

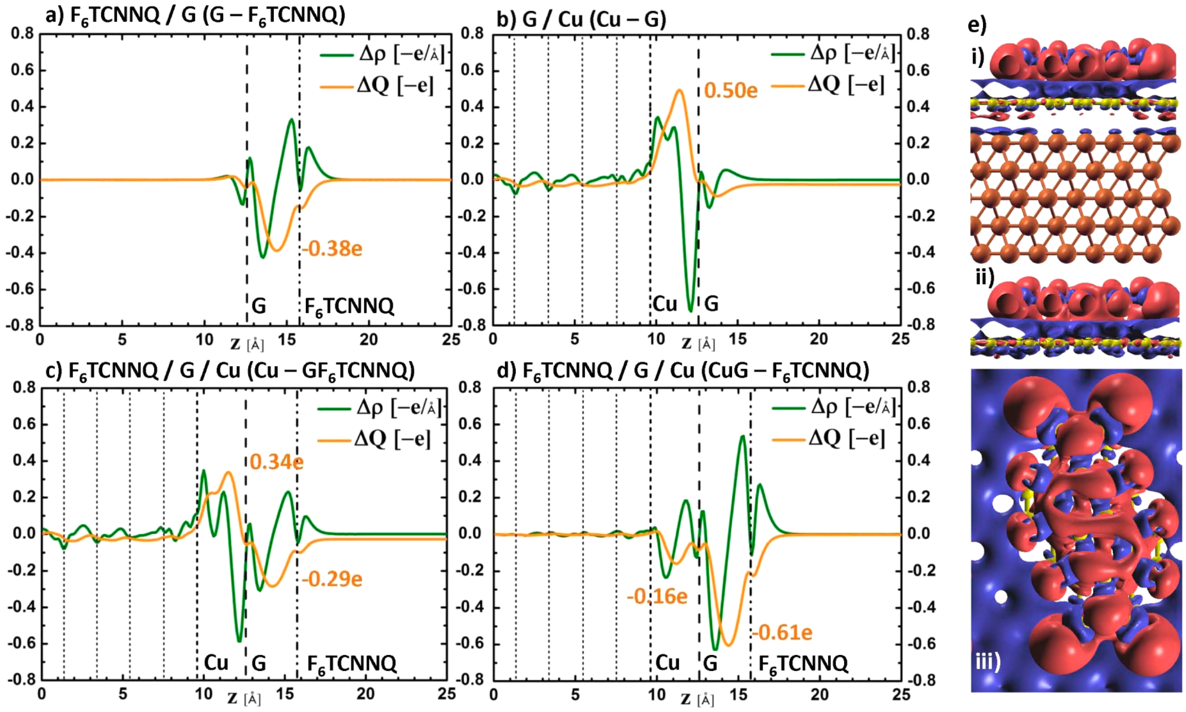

Figure 10. Plane average differential charge density (DCD), $\Delta\rho\ (z)$ (green), charge transfer amount, $\Delta Q(z)$ (orange), for (a) F6TCNNQ adsorbed on graphene, (b) graphene on Cu, (c) F6TCNNQ on graphene and then adsorbed on Cu, and (d) graphene on Cu and then with F6TCNNQ adsorbed. Side view DCD isosurface for F_6TCNNQ adsorbed on graphene [e(i)] and graphene-on-copper [e(ii)] and top view DCD isosurface for F_6TCNNQ adsorbed on graphene [e(iii)]. Regions in red correspond to negatively charged populations, and regions in blue correspond to positively charged populations. The amount of charge transfer is indicated in each plot. Parentheses indicate the subsystems used for the DCDs. Short dashed lines indicate the copper layers; dashed lines indicate the graphene layer, and double dotted dashed lines indicate the F_6TCNNQ layer.

features of the LUMO (L*) and HOMO (H*) of F_6TCNNQ, and the LUMO of the molecule is pinned close to E_F after adsorption on graphene. Such a pinning results from CT between the graphene and the molecule that occurs in order to bring the system into electronic equilibrium. The electron transfer from graphene to F_6TCNNQ, i.e., p-doping of graphene (the amount of CT reaches $\sim -0.38e$ $\{-0.23e/\text{nm}^2\}$, with e being the elementary charge of one electron obtained by a differential charge density (DCD) calculation), is visualized in the charge density plot in Figure 10a. The energy gap between H* and L* (ΔE = 0.9 eV) perfectly agrees with the experimental value obtained by UPS (ΔE = 0.9 eV; see Figure 2c,f).

To identify how the contact with the metallic substrate interferes with the CT mechanism at the graphene−molecule interface, the DFT simulations were repeated for graphene placed on top of 5 layers of Cu(111). The band structures of the resulting unit cells are shown in Figure 9. In the case of G/Cu (see Figure 9b), the DFT calculations show that the Dirac point of graphene does not coincide with the Fermi level of the metal; rather, it is located 0.5 eV below E_F (see red circle in Figure 9b). As is nicely explained in refs 29 and 30, in graphene−metal contacts, charge transfer is a secondary effect. The main effect is the downward shift of graphene's energy levels due to the Pauli exclusion principle,[30,31] which takes place between the metal atoms' outermost s-electrons and graphene's π-electrons. Thus, graphene can be n-doped when its charge neutrality level is relatively shifted down below the metals' Fermi level, which seems to be the case for copper.

Next, the F$_6$TCNNQ molecules were physisorbed on graphene-on-copper G/Cu (Figure 9d). The size of the supercells used for the calculations was 17.2 × 9.9 × 40 Å^3. The interaction energy in this case is larger compared to the case of graphene in vacuum (1.05 eV/nm^2), i.e., 1.39 eV/nm^2. The molecule lies slightly closer, 3.18 Å over graphene, with the distance between the nitrogen atoms of the cyano groups and graphene even smaller, 3.03 Å. In this case, the molecule bends gently toward graphene (Figure S5). Noteworthy, while the presence of the electron acceptors shifts the Dirac point by ∼0.44 eV *above* the Fermi level in freestanding graphene corresponding to p-doping, the position of the Dirac cone is hardly affected (by less than ∼0.05 eV) in the G/Cu case. In the corresponding ternary system, a detailed analysis of the electronic band structure places the Dirac point ∼0.45 eV *below* E_F (see red circle in Figure 9d). Compared to G/Cu alone, now graphene is still n-doped, however, to a slightly lesser extent. This might seem at first glance surprising as the graphene layer is in contact with the electron poor F$_6$TCNNQ molecules. From close inspection of the electronic band structure and charge density plots, the picture that emerges shows that the electron density is *in fact* mainly due to the larger (compared to graphene) Cu electron reservoir, through the sandwiched graphene layer. This is best understood from the differential charge density (DCD) plots computed for two partitioning schemes in Figure 10c,d. In the first partitioning scheme, the fragments used to compute the DCD are Cu on one hand and the graphene interacting with F$_6$TCNNQ on the other hand. Figure 10c is reminiscent of Figure 10b,a and dominated by the charge redistribution induced by the pillow effect at the Cu−G interface and the increased electronic density over the acceptor monolayer. In the second partitioning scheme, Figure 10d, the fragments are instead graphene plus Cu and F$_6$TCNNQ. As the Pauli repulsion is mostly induced by the graphene layer in contact with the metal and only weakly affected by the molecular doping layer atop, the use of these fragments in the calculation of charge density differences emphasizes contributions from electron transfer over changes in electronic density induced by Pauli repulsion effects. Figure 10d clearly points to an increased charge density around graphene (masked by the Pauli effects in Figure 10c), in line with n-doping of the graphene interlayer as assessed from the relative position of the Dirac cone below the Fermi level, *vide supra*. The CT that thus occurs from copper to the combined graphene-adlayer system generates an electric field across the graphene, and therefore, its states are shifted to lower binding energy, as is indeed experimentally observed (experimental shift of 0.4 eV toward lower BE in the C 1s core level; see Figure 3e). The increased amount of CT ($-0.61e$ {$-0.37e$/nm^2}, obtained by a differential charge density (DCD) calculation) to the acceptors on the G/Cu substrate, which is significantly larger compared to the corresponding CT in the free-standing G layer ($-0.38e$ {$-0.23e$/nm^2}), further explains the experimental prominence of only negatively charged F$_6$TCNNQ in the N 1s core level of G/Cu (see Figure 3f) up to θ = 0.4 nm, that is considered to be the first filled monolayer. It can also explain the increase in the interaction energy between adsorbent and adsorbate. In addition, the total work function change, $\Delta\Phi$ = 1.3 eV, is in very good agreement with the experimental value. Thus, the calculated vacuum level shift in this case, ΔE_{vac} = 1.25 eV ($\Delta E_{\mathrm{vac}} = \Delta\Phi - \Delta E_F$), is higher, as it involves a larger and longer distance electron transfer.

Figure 10e(iii) represents a top view of the DCD isosurface for the molecule adsorbed on graphene. This charge density distribution further shows that the charge is mainly localized at the CN groups, explaining the absence of any energy shift in the F 1s core level spectra (Figure 3c,g). Assuming the same growth mode on both supports Qu and Cu (as evidenced by UPS and XPS), a larger number of molecules in the monolayer can withdraw electrons from the metallic Cu substrate (considering that it is an infinite electron reservoir compared to graphene). This is in agreement with the experimental observation of the N 1s core level spectra that 50% of the molecules are charged in the monolayer for G/Qu (see Figure 3b), whereas ∼100% are charged in the monolayer for G/Cu (see Figure 3f). This increased amount of CT, together with the fact that electrons are actually withdrawn from Cu, explains the higher $\Delta\Phi$ observed for G/Cu (1.3 eV) compared to G/Qu (1.0 eV). In the G/Cu case, the dipole formed between the negative charge in the molecule and the positive image charge in the metal is larger, since the distance between the charges is longer. Furthermore, the number of such dipoles per surface area is higher since more molecules become charged. In the G/Qu case, where the transferred charge originates from graphene, this dipole is smaller since (a) the molecule−graphene distance is shorter and (b) fewer molecules get charged per unit area.

Figure 11 summarizes the energy shifts of the C 1s core level and the work function Φ observed for F$_6$TCNNQ/G/Qu and

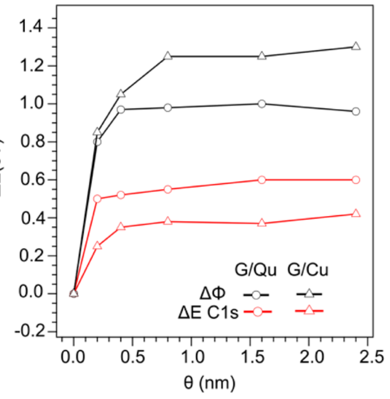

Figure 11. Work function and C 1s core level shifts upon deposition of F$_6$TCNNQ on graphene-on-quartz (G/Qu) and graphene-on-copper (G/Cu).

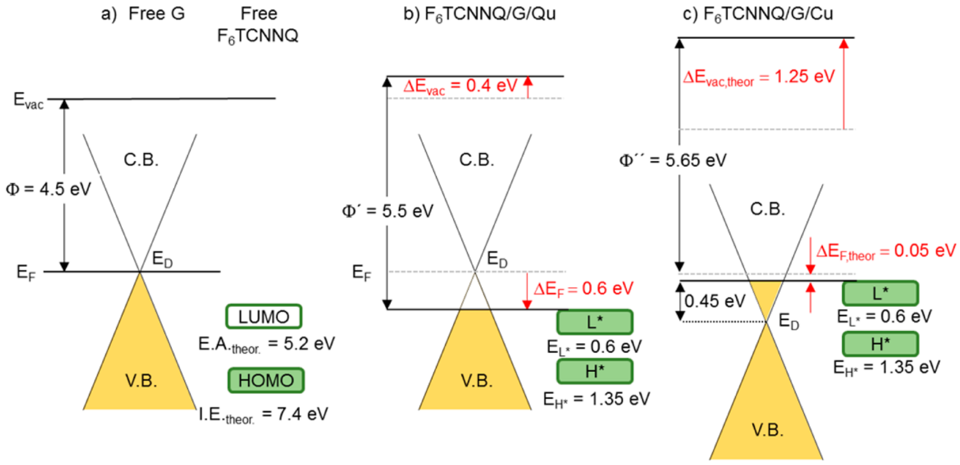

Figure 12. Energy level diagram for (a) free graphene (G) and free F_6TCNNQ, (b) $F_6TCNNQ/G/Qu$ interface, and (c) $F_6TCNNQ/G/Cu$ interface. In (a), the electron affinity (E.A.) and the ionization energy (I.E.) are calculated for the gas phase (free) molecule before contact with graphene. In (b) and (c), the energy positions of the (partially) populated LUMO (L*) at $E_L^* = 0.6$ eV and of the relaxed HOMO (H*) at $E_H = 1.35$ eV are derived from the experimental data. Φ corresponds to the work function; E_{vac} is the vacuum energy level. E_F is the Fermi level; E_D is the Dirac point of graphene. C.B. and V.B. are the conduction and valence band of graphene. The values are experimentally obtained unless otherwise indicated (theor.).

$F_6TCNNQ/G/Cu$ as a function of F_6TCNNQ coverage. In addition to the *higher* work function increase for G/Cu compared to G/Qu ($\Delta\Phi = 1.3$ eV versus 1.0 eV at $\theta = 2.4$ nm), a *smaller* C 1s core level shift is observed for G/Cu ($\Delta E_{C\ 1s} =$ 0.4 eV versus 0.6 eV), which is understandable from the fact that it is due to the potential drop across graphene and *not* due to a shift of E_F (doping). Figure 12 shows a simplified valence energy level diagram before and after the formation of the interface for the case of F_6TCNNQ physisorbed on G/Cu and G/Qu. To position the frontier molecular levels of F_6TCNNQ, the calculated DFT gas phase values of the ionization energy (7.4 eV) and electron affinity (5.2 eV) were used.

(i) In the G/Qu case, the measured initial work function of graphene is $\Phi = 4.5$ eV (Figure 2a). The calculated work function of graphene is 4.42 eV. After contact, a shift in E_F is observed, since doping of the graphene sheet occurs, lowering E_F by $\Delta E_F \approx 0.6$ eV, as measured experimentally (the calculated shift is 0.44 eV). The remaining work function increase results from an upward vacuum level shift due to the reorganization of positive and negative charges giving rise to a dipole at the interface between F_6TCNNQ and G, which yields an additional shift of ~0.4 eV (~0.66 eV) as measured (calculated). The overall change in work function is $\Delta\Phi$ = 1.0 eV (1.1 eV) from measurements (calculations).

(ii) In the G/Cu case, the measured (calculated) initial work function of graphene is lowered to 4.35 eV (3.93 eV) due to n-doping. Quite interestingly, the graphene layer remains n-doped even when in direct contact with the overlaid F_6TCNNQ acceptors, with additional electronic density being transferred from the vast metal electron reservoir through graphene. As a result, the Dirac point shifts marginally, but the larger amplitude and longer distance electron transfer from Cu to F_6TCNNQ is accompanied by a very large vacuum level shift that accounts for more than 95% of the total work function shift, $\Delta\Phi$ = 1.3 eV from both measurements and calculations.

■ CONCLUSION

Using UPS, XPS, and XAS together with DFT calculations, we provided detailed insight into the interaction of molecularly modified graphene supported by insulating quartz versus metallic copper. We observe a large $\Delta\Phi$ increase of 1.0 eV when the molecular acceptor F_6TCNNQ is deposited onto G/Qu. The Φ increase is even higher (1.3 eV) when the underlying substrate is G/Cu. For G/Qu, the technologically relevant substrate, we could deconvolute the $\Delta\Phi$ into two contributions: (a) surface charge transfer p-doping of graphene that gives a $\Delta\Phi$ = 0.6 eV and (b) dipole formation at the F_6TCNNQ/G interface, resulting from the charge reorganization that gives a further $\Delta\Phi$ = 0.4 eV. The CT was confirmed by XPS. In the case of G/Cu, the transferred charge mainly originates from the Cu substrate supporting graphene; thus, after the CT, the doping level of graphene remains essentially unchanged and of n-type. In that case, a dipole moment and thus an electrostatic field is created between the molecule and the Cu that consequently shifts the energy levels of graphene that is located in this electrostatic field, as observed in the C 1s core level of G/Cu. Finally, we would like to emphasize that the hybrid system $F_6TCNNQ/G/Qu$ can be used as a transparent electrode that is highly conducting, since the graphene's sp^2 network is only weakly perturbed after physisorption of F_6TCNNQ. Furthermore, it provides a p-doped graphene layer with a work function that matches the frontier energy levels of transport materials commonly used in many (opto-)electronic devices. When, instead, a Cu substrate is used, the work function is *increased* even further (by ~1.3 eV), *albeit the fact graphene is n-doped*. Therefore, this n-doped graphene, and generally any molecular-acceptor-modified n-type graphene, can yet be employed for hole injection into (organic) semiconductors in devices.

■ METHODS

Material Preparations and Characterizations. Graphene was synthesized by chemical vapor deposition on G/Cu at a substrate temperature of 1000 °C and then transferred to quartz using a wet transfer procedure.[11,12] The as-received graphene-coated quartz was further annealed in ultrahigh vacuum (UHV, base pressure 10^{-10}

mbar) at 600 °C for 24 h to desorb residual poly(methylmethacrylate) (PMMA), which was used as a rigid support of graphene during the wet transfer. The resulting graphene/quartz samples are denoted as G/Qu. F_6TCNNQ was deposited onto graphene in UHV by sublimation from resistively heated quartz crucibles in a preparation chamber (base pressure $<5 \times 10^{-9}$mbar) directly connected to the analysis chamber (base pressure $<1 \times 10^{-10}$ mbar). The nominal film thickness (i.e., mass−thickness read of the microbalance, irrespective of actual film morphology) was monitored using a calibrated quartz-crystal microbalance, and the density used for the organic material was 1.6 g/cm^3. The purity and chemical structure of the transferred CVD graphene-on-quartz after prolonged annealing in UHV was confirmed by XPS, as reported previously.[18,32]

Experimental. XPS and UPS measurements were performed at the end station SurICat (PM4) at the BESSY II synchrotron light source (Berlin, Germany). The excitation energies used for C 1s and N 1s core level analysis were 390 and 505 eV, respectively, to achieve the same photoelectron escape depth of ∼1 nm[33] with a spectral energy resolution of 300 meV. The photon energy and the resolution for UPS were 35 and 150 meV, respectively. We checked for possible beam degradation by frequently monitoring the core-level peaks of the molecules after prolonged exposure (more than 2 h). No apparent change was observed in the core-level peaks, which confirmed the negligible photon beam damage under the low beam current used. Sample charging was ruled out by checking the binding energy of the C 1s of the G/Qu sample. For obtaining the secondary electron cutoff (SECO) spectra, the samples were biased at −10 V with respect to the electron analyzer. The energy positions of the SECOs were obtained by linear extrapolation of the SECO peaks at half-maximum toward the background. The deconvolution of the XPS spectra was performed using a Shirley background and Voigt peak lineshapes. The XAS experiments were performed at the BEAR end station (BL8.1L), at the left exit of the 8.1 bending magnet of the ELETTRA synchrotron facility (Trieste, Italy).[34,35] All XAS spectra were collected in total electron yield (TEY) mode (i.e., drain current mode) at the N K-edge and normalized to the incident photon flux and to the clean substrate signal. The spectral energy was calibrated by referring to CO_2 C 1s−π^* transitions. The incidence angle of the light with respect to the sample surface plane was kept fixed at 10°, and the sample was then rotated around the beam axis to change the polarization from s to p. This leads to an effective rotation of the electric field plane at the surface while keeping the excitation volume constant. In order to keep both the illuminated area (i.e., the excited volume) and the incidence angle constant, we changed the direction of the electric field vector $\vec{E}$ from perpendicular to parallel with respect to the scattering plane. This was achieved by rotating the chamber angle ψ_c with respect to the beam axis from $\psi_c = 0°$ (s-scattering) to $\psi_c = 90°$ (p-scattering).[29] The synchrotron beam was linearly polarized (ellipticity $\varepsilon = |\overrightarrow{E_V}|^2/|\overrightarrow{E_H}|^2 = 0.1$, where V (H) is the vertical (horizontal) direction and $\varepsilon = 1$ (0) for circularly (linearly) polarized light). In order to correctly process the acquired data, each absorption spectrum collected at different angle ψ_c was normalized to the absorption spectrum acquired under the same experimental conditions and the energy range, on an Au(111) sputtered (i.e., carbon free) sample. The energy scale of each single spectrum was recalibrated taking into account the energy fluctuation of characteristic absorption features measured on the refocusing mirror.

Simulations. The XAS simulations were performed on the free molecule using the Slater transition state method using the StoBe DFT simulation code.[36−38] Angle-dependent dipole transitions and absorption at the N K-edge were calculated for the equivalent N centers. To better describe relaxation effects, an IGLO-III basis set was used on each excitation center, while effective core potentials were used for the remaining N atoms. The calculated dipole-excitation spectra were Gaussian convoluted with an energy-dependent broadening and rigidly shifted by −1.7 eV to align to the experimental curves. For the charged molecule, XAS was simulated assuming an additional electron charge on the molecule. Valence band calculations were carried out with the Vienna Ab initio Simulation Package (VASP)[39−41] and SIESTA[42] software. Optimization of the structures were done with VASP, using the Perdew−Burke−Ernzerhof (PBE) exchange-correlation functional, a plane-wave basis set with an energy cutoff of 400 eV, and the tetrahedron method with Blöchl corrections for the partial occupancies, with smearing of 0.05 eV. Grimme-type (DFT-D) dispersion corrections were applied,[43] since van der Waals interactions play a significant role in noncovalent functionalization. The whole system (graphene and molecule) was optimized until the remaining atomic forces were smaller than 0.02 eV/Å in a supercell with dimensions 17.1 × 9.9 × 30 Å^3 using a k-point mesh of 5 × 5 × 1. In the case of physisorption on graphene-on-copper; the supercell was 17.2 × 9.9 × 40 Å using a k-point mesh of 5 × 5 × 1. The three bottom layers of the metallic substrate (total of 5 layers) were frozen during optimization. The plane average charge density (DCD) and the charge transfer amount ($\Delta Q(z)$) were calculated from the difference in charge density between the system and the two subsystems, i.e., "charge density of Gr-F6" − "charge density of "Gr" − "charge density of F6". The density of states (DOS) plots we produced using the optimized structures with a five times denser k-point mesh. Local density of states (LDOS) was also performed around the peaks appearing after interaction with the molecule. LDOS was calculated in a region of 0.2 eV (peak energy ±0.1 eV). Band structures for all systems were created with SIESTA, from the optimized VASP structures. The PBE exchange-correlation functional was used with the Double Zeta Polarized (DZP) basis set. All the 3D isodensity representations in this work were produced by XCrysDen.[44]

■ ASSOCIATED CONTENT

Ⓢ Supporting Information

The Supporting Information is available free of charge on the ACS Publications website at DOI: 10.1021/acsami.5b04777.

> Structural information about the neutral and charged F_6TCNNQ molecule in the gas phase and the molecule physisorbed on graphene in vacuum and on graphene-on-copper, as obtained by DFT calculations; the technique used to obtain the differential charge density plots (Figure 10) (PDF)

■ AUTHOR INFORMATION

Corresponding Authors

*E-mail: david.beljonne@umons.ac.be.
*E-mail: norbert.koch@physik.hu-berlin.de.

Author Contributions

$^\nabla$C.C. and A.G. contributed equally.

Notes

The authors declare no competing financial interest.

■ ACKNOWLEDGMENTS

The authors acknowledge funding from the 7th Marie Curie ITN GENIUS program. Research in Mons is also supported by the OPTI2MAT Excellence Program of Région Wallone and FNRS/FRFC. D.B. is a research director of the Fonds National de la Recherche Scientifique-FNRS. Research in Berlin was further supported by the DGF (SFB951) and the Helmholtz Energy Alliance "Hybrid Photovoltaics".

■ REFERENCES

(1) Novoselov, K. S.; Jiang, D.; Schedin, F.; Booth, T. J.; Khotkevich, V. V.; Morozov, S. V.; Geim, A. K. Two-Dimensional Atomic Crystals. *Proc. Natl. Acad. Sci. U. S. A.* **2005**, *102* (30), 10451−10453.

(2) Novoselov, K. S.; Geim, A. K.; Morozov, S. V.; Jiang, D.; Katsnelson, M. I.; Grigorieva, I. V.; Dubonos, S. V.; Firsov, A. A. Two-Dimensional Gas of Massless Dirac Fermions in Graphene. *Nature* **2005**, *438* (7065), 197−200.

(3) Geim, A. K.; Novoselov, K. S. The Rise of Graphene. *Nat. Mater.* **2007**, *6* (3), 183−191.

(4) Castro Neto, A. H.; Guinea, F.; Peres, N. M. R.; Novoselov, K. S.; Geim, A. K. The Electronic Properties of Graphene. *Rev. Mod. Phys.* **2009**, *81* (1), 109−162.

(5) Lee, C.; Wei, X.; Kysar, J. W.; Hone, J. Measurement of the Elastic Properties and Intrinsic Strength of Monolayer Graphene. *Science* **2008**, *321* (5887), 385−388.

(6) Han, T.-H.; Lee, Y.; Choi, M.-R.; Woo, S.-H.; Bae, S.-H.; Hong, B. H.; Ahn, J.-H.; Lee, T.-W. Extremely Efficient Flexible Organic Light-Emitting Diodes with Modified Graphene Anode. *Nat. Photonics* **2012**, *6* (2), 105−110.

(7) Schedin, F.; Geim, A. K.; Morozov, S. V.; Hill, E. W.; Blake, P.; Katsnelson, M. I.; Novoselov, K. S. Detection of Individual Gas Molecules Adsorbed on Graphene. *Nat. Mater.* **2007**, *6* (9), 652−655.

(8) Wang, X.; Zhi, L.; Muellen, K. Transparent, Conductive Graphene Electrodes for Dye-Sensitized Solar Cells. *Nano Lett.* **2008**, *8* (1), 323−327.

(9) Yoo, E.; Kim, J.; Hosono, E.; Zhou, H.; Kudo, T.; Honma, I. Large Reversible Li Storage of Graphene Nanosheet Families for Use in Rechargeable Lithium Ion Batteries. *Nano Lett.* **2008**, *8* (8), 2277−2282.

(10) Bae, S.; Kim, H.; Lee, Y.; Xu, X.; Park, J.-S.; Zheng, Y.; Balakrishnan, J.; Lei, T.; Kim, H. R.; Song, Y. I.; Kim, Y.-J.; Kim, K. S.; Özyilmaz, B.; Ahn, J.-H.; Hong, B. H.; Iijima, S. Roll-to-Roll Production of 30-Inch Graphene Films for Transparent Electrodes. *Nat. Nanotechnol.* **2010**, *5* (8), 574−578.

(11) Li, X.; Cai, W.; An, J.; Kim, S.; Nah, J.; Yang, D.; Piner, R.; Velamakanni, A.; Jung, I.; Tutuc, E.; Banerjee, S. K.; Colombo, L.; Ruoff, R. S. Large-Area Synthesis of High-Quality and Uniform Graphene Films on Copper Foils. *Science* **2009**, *324* (5932), 1312−1314.

(12) Li, X.; Zhu, Y.; Cai, W.; Borysiak, M.; Han, B.; Chen, D.; Piner, R. D.; Colombo, L.; Ruoff, R. S. Transfer of Large-Area Graphene Films for High-Performance Transparent Conductive Electrodes. *Nano Lett.* **2009**, *9* (12), 4359−4363.

(13) Chen, W.; Chen, S.; Qi, D. C.; Gao, X. Y.; Wee, A. T. S. Surface Transfer P-Type Doping of Epitaxial Graphene. *J. Am. Chem. Soc.* **2007**, *129* (34), 10418−10422.

(14) Coletti, C.; Riedl, C.; Lee, D. S.; Krauss, B.; Patthey, L.; von Klitzing, K.; Smet, J. H.; Starke, U.; von Klitzing, K. Charge Neutrality and Band-Gap Tuning of Epitaxial Graphene on SiC by Molecular Doping. *Phys. Rev. B: Condens. Matter Mater. Phys.* **2010**, *81* (23), 235401.

(15) Wang, Q. H.; Hersam, M. C. Room-Temperature Molecular-Resolution Characterization of Self-Assembled Organic Monolayers on Epitaxial Graphene. *Nat. Chem.* **2009**, *1* (3), 206−211.

(16) Barja, S.; Garnica, M.; Hinarejos, J. J.; Vázquez de Parga, A. L.; Martín, N.; Miranda, R. Self-Organization of Electron Acceptor Molecules on Graphene. *Chem. Commun.* **2010**, *46* (43), 8198.

(17) Dong, X.; Fu, D.; Fang, W.; Shi, Y.; Chen, P.; Li, L.-J. Doping Single-Layer Graphene with Aromatic Molecules. *Small* **2009**, *5* (12), 1422−1426.

(18) Christodoulou, C.; Giannakopoulos, A.; Nardi, M. V.; Ligorio, G.; Oehzelt, M.; Chen, L.; Pasquali, L.; Timpel, M.; Giglia, A.; Nannarone, S.; Norman, P.; Linares, M.; Parvez, K.; Müllen, K.; Beljonne, D.; Koch, N. Tuning the Work Function of Graphene-on-Quartz with a High Weight Molecular Acceptor. *J. Phys. Chem. C* **2014**, *118* (9), 4784−4790.

(19) Kong, L.; Enders, A.; Rahman, T. S.; Dowben, P. A. Molecular Adsorption on Graphene. *J. Phys.: Condens. Matter* **2014**, *26*, 443001.

(20) Koch, N.; Duhm, S.; Rabe, J. P.; Vollmer, A.; Johnson, R. L. Optimized Hole Injection with Strong Electron Acceptors at Organic-Metal Interfaces. *Phys. Rev. Lett.* **2005**, *95* (23), 237601.

(21) Tietze, M. L.; Burtone, L.; Riede, M.; Lüssem, B.; Leo, K. Fermi Level Shift and Doping Efficiency in P-Doped Small Molecule Organic Semiconductors: A Photoelectron Spectroscopy and Theoretical Study. *Phys. Rev. B: Condens. Matter Mater. Phys.* **2012**, *86* (3), 035320.

(22) Koech, P. K.; Padmaperuma, A. B.; Wang, L.; Swensen, J. S.; Polikarpov, E.; Darsell, J. T.; Rainbolt, J. E.; Gaspar, D. J. Synthesis and Application of 1,3,4,5,7,8-Hexafluorotetracyanonaphthoquinodimethane (F6-TNAP): A Conductivity Dopant for Organic Light-Emitting Devices. *Chem. Mater.* **2010**, *22* (13), 3926−3932.

(23) Lüssem, B.; Tietze, M. L.; Kleemann, H.; Hoßbach, C.; Bartha, J. W.; Zakhidov, A.; Leo, K. Doped Organic Transistors Operating in the Inversion and Depletion Regime. *Nat. Commun.* **2013**, *4* (2775), 1−6.

(24) Chen, W.; Qi, D.; Gao, X.; Wee, A. T. S. Surface Transfer Doping of Semiconductors. *Prog. Surf. Sci.* **2009**, *84* (9−10), 279−321.

(25) Meyer, J.; Kidambi, P. R.; Bayer, B. C.; Weijtens, C.; Kuhn, A.; Centeno, A.; Pesquera, A.; Zurutuza, A.; Robertson, J.; Hofmann, S. Metal Oxide Induced Charge Transfer Doping and Band Alignment of Graphene Electrodes for Efficient Organic Light Emitting Diodes. *Sci. Rep.* **2014**, *4* (5380), 1−7.

(26) Chen, Z.; Santoso, I.; Wang, R.; Xie, L. F.; Mao, H. Y.; Huang, H.; Wang, Y. Z.; Gao, X. Y.; Chen, Z. K.; Ma, D.; Wee, A. T. S.; Chen, W. Surface Transfer Hole Doping of Epitaxial Graphene Using MoO[sub 3] Thin Film. *Appl. Phys. Lett.* **2010**, *96* (21), 213104.

(27) Heimel, G.; Duhm, S.; Salzmann, I.; Gerlach, A.; Strozecka, A.; Niederhausen, J.; Bürker, C.; Hosokai, T.; Fernandez-Torrente, I.; Schulze, G.; Winkler, S.; Wilke, A.; Schlesinger, R.; Frisch, J.; Bröker, B.; Vollmer, A.; Detlefs, B.; Pflaum, J.; Kera, S.; Franke, K. J.; Ueno, N.; Pascual, J. I.; Schreiber, F.; Koch, N. Charged and Metallic Molecular Monolayers through Surface-Induced Aromatic Stabilization. *Nat. Chem.* **2013**, *5* (3), 187−194.

(28) Duhm, S.; Heimel, G.; Salzmann, I.; Glowatzki, H.; Johnson, R. L.; Vollmer, A.; Rabe, J. P.; Koch, N. Orientation-Dependent Ionization Energies and Interface Dipoles in Ordered Molecular Assemblies. *Nat. Mater.* **2008**, *7* (4), 326−332.

(29) Serkovic Loli, L. N.; Hamoudi, H.; Gayone, J. E.; Martiarena, M. L.; Sánchez, E. A.; Grizzi, O.; Pasquali, L.; Nannarone, S.; Doyle, B. P.; Dablemont, C.; Esaulov, V. A. Growth of N, N ′-Bis(1-Ethylpropyl)-perylene-3,4,9,10-Tetracarboxdiimide Films on Ag (111). *J. Phys. Chem. C* **2009**, *113* (41), 17866−17875.

(30) Giovannetti, G.; Khomyakov, P.; Brocks, G.; Karpan, V.; van den Brink, J.; Kelly, P. Doping Graphene with Metal Contacts. *Phys. Rev. Lett.* **2008**, *101* (2), 026803.

(31) Gong, C.; Lee, G.; Shan, B.; Vogel, E. M.; Wallace, R. M.; Cho, K. First-Principles Study of Metal−graphene Interfaces. *J. Appl. Phys.* **2010**, *108* (12), 123711.

(32) Pirkle, A.; Chan, J.; Venugopal, A.; Hinojos, D.; Magnuson, C. W.; McDonnell, S.; Colombo, L.; Vogel, E. M.; Ruoff, R. S.; Wallace, R. M. The Effect of Chemical Residues on the Physical and Electrical Properties of Chemical Vapor Deposited Graphene Transferred to SiO2. *Appl. Phys. Lett.* **2011**, *99* (12), 122108.

(33) Cumpson, P. J.; Seah, M. P. Elastic Scattering Corrections in AES and XPS. II. Estimating Attenuation Lengths and Conditions Required for Their Valid Use in Overlayer/Substrate Experiments. *Surf. Interface Anal.* **1997**, *25* (6), 430−446.

(34) Pasquali, L.; De Luisa, A.; Nannarone, S. The UHV Experimental Chamber for Optical Measurements (Reflectivity and Absorption) and Angle Resolved Photoemission of the BEAR Beamline at ELETTRA. In *AIP Conference Proceedings*; AIP: Melville, NY, 2004; Vol. *705*, pp 1142−1145.

(35) Nannarone, S.; Borgatti, F.; DeLuisa, A.; Doyle, B. P.; Gazzadi, G. C.; Giglia, A.; Finetti, P.; Mahne, N.; Pasquali, L.; Pedio, M.; Selvaggi, G.; Naletto, G.; Pelizzo, M. G.; Tondello, G. The BEAR Beamline at Elettra. In *AIP Conference Proceedings*; AIP: Melville, NY, 2004; Vol. *705*, pp 450−453.

(36) Hermann, K.; Pettersson, L. G. M.; Casida, M. E.; Daul, C.; Hermann, A.; Pettersson, L. G. M.; Casida, M. E.; Daul, C.; Goursot, A.; Koester, A.; Proynov, E.; St-Amant, A.; Salahub, D. R. *StoBe-deMon*, Version 3.0; 2007 ; www.fhi-berlin.mpg.de/KHsoftware/StoBe/StoBeMAN.html.

(37) Slater, J. C.; Johnson, K. H. Self-Consistent-Field Xα Cluster Method for Polyatomic Molecules and Solids. *Phys. Rev. B* **1972**, *5* (3), 844−853.

(38) Slater, J. C.; Loewdin, P. O. E. . *Advances in Quantum Chemistry*; Academic Press: New York, 1972.

(39) Kresse, G.; Hafner, J. Ab Initio Molecular Dynamics for Liquid Metals. *Phys. Rev. B: Condens. Matter Mater. Phys.* **1993**, *47* (1), 558−561.

(40) Kresse, G.; Furthmüller, J. Efficient Iterative Schemes for Ab Initio Total-Energy Calculations Using a Plane-Wave Basis Set. *Phys. Rev. B: Condens. Matter Mater. Phys.* **1996**, *54* (16), 11169−11186.

(41) Kresse, G.; Furthmüller, J. Efficiency of Ab-Initio Total Energy Calculations for Metals and Semiconductors Using a Plane-Wave Basis Set. *Comput. Mater. Sci.* **1996**, *6* (1), 15−50.

(42) Soler, J. M.; Artacho, E.; Gale, J. D.; García, A.; Junquera, J.; Ordejón, P.; Sánchez-Portal, D. The SIESTA Method for Ab Initio Order-N Materials Simulation. *J. Phys.: Condens. Matter* **2002**, *14* (11), 2745.

(43) Grimme, S. Semiempirical GGA-Type Density Functional Constructed with a Long-Range Dispersion Correction. *J. Comput. Chem.* **2006**, *27* (15), 1787−1799.

(44) Kokalj, A. Computer Graphics and Graphical User Interfaces as Tools in Simulations of Matter at the Atomic Scale. *Comput. Mater. Sci.* **2003**, *28* (2), 155−168.